This is a repository copy of *Extended Kalman Filtering Projection Method to Reduce the 3σ Noise Value of Optical Biosensors*.

White Rose Research Online URL for this paper:
https://eprints.whiterose.ac.uk/168561/

Version: Published Version

Article:

Li, Kezheng, Gupta, Roopam, Drayton, Alexander et al. (5 more authors) (2020) Extended Kalman Filtering Projection Method to Reduce the 3σ Noise Value of Optical Biosensors. ACS sensors. pp. 3474-3482. ISSN 2379-3694

https://doi.org/10.1021/acssensors.0c01484

Article

Extended Kalman Filtering Projection Method to Reduce the 3σ Noise Value of Optical Biosensors

Kezheng Li,* Roopam Gupta, Alexander Drayton, Isabel Barth, Donato Conteduca, Christopher Reardon, Kishan Dholakia, and Thomas F. Krauss

Cite This: *ACS Sens.* 2020, 5, 3474−3482

Read Online

ACCESS | Metrics & More | Article Recommendations | SI Supporting Information

ABSTRACT: Optical biosensors have experienced a rapid growth over the past decade because of their high sensitivity and the fact that they are label-free. Many optical biosensors rely on tracking the change in a resonance signal or an interference pattern caused by the change in refractive index that occurs upon binding to a target biomarker. The most commonly used method for tracking such a signal is based on fitting the data with an appropriate mathematical function, such as a harmonic function or a Fano, Gaussian, or Lorentz function. However, these functions have limited fitting efficiency because of the deformation of data from noise. Here, we introduce an extended Kalman filter projection (EKFP) method to address the problem of resonance tracking and demonstrate that it improves the tolerance to noise, reduces the 3σ noise value, and lowers the limit of detection (LOD). We utilize the method to process the data of experiments for detecting the binding of C-reactive protein in a urine matrix with a chirped guided mode resonance sensor and are able to improve the LOD from 10 to 1 pg/mL. Our method reduces the 3σ noise value of this measurement compared to a simple Fano fit from 1.303 to 0.015 pixels. These results demonstrate the significant advantage of the EKFP method to resolving noisy data of optical biosensors.

KEYWORDS: optical biosensors, signal processing, signal-to-noise ratio, extended Kalman filter, guided mode resonance, microring resonator
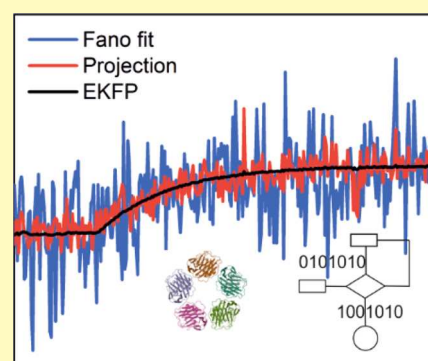
Optical refractive index biosensors are widely researched because of their high sensitivity and their intrinsic simplicity with no requirement of fluorescent labels. Many different types of optical biosensors have been reported, based on the principles of surface plasmon resonances (SPR),[1] microring resonances,[2] dual mode[3] or Mach−Zehnder interferences,[4] porous silicon nanostructures,[5] photonic crystals,[6] or guided mode resonances (GMRs).[7−9] The unifying feature of all of these modalities is that the resonance signal is recorded, fitted to a mathematical function, and tracked as a function of time, for example, to record a protein−protein binding curve. The limit of detection (LOD) is then determined from the noise limit of the measurement. It is not surprising that the exact mechanism of curve fitting and tracking has a significant influence on the noise limit that can be obtained.

Curve fitting is particularly difficult for low Q resonances such as SPRs and GMRs. Therefore, a number of more advanced fitting methods have been developed. These include the centroid and full width at half-maximum method,[10] locally weighted parametric regression,[11] polynomial curve fitting,[12] and principal component analysis (PCA).[13,14] It is difficult to compare these methods directly from the literature because of differences in experimental arrangements, but the stated experimental error is typically around 10⁻⁴ RIU.[15] The double

projection method[16] was introduced more recently and has been shown to be more accurate in the determination of the resonance position with an estimated error around 2.2×10^{-5} RIU. This method uses eigenvector analysis to compare the measurement with simulated results, then solving the unknown refractive index by projecting the vectors to the basis twice. Because the eigenvector analysis is based on a singular value decomposition, the algorithm relies on a large matrix operation which is computationally expensive and experimentally rather complex. However, a simpler one-step projection method was subsequently introduced by Abumazwed et al.[17] with a slightly worse stated LOD of 7.5×10^{-4} RIU. The one-step projection method is attractive because it eliminates the use of the eigenvector analysis, directly convoluting the measured spectrum with the simulated spectrum database, which reduces the computational complexity by more than 2 orders.
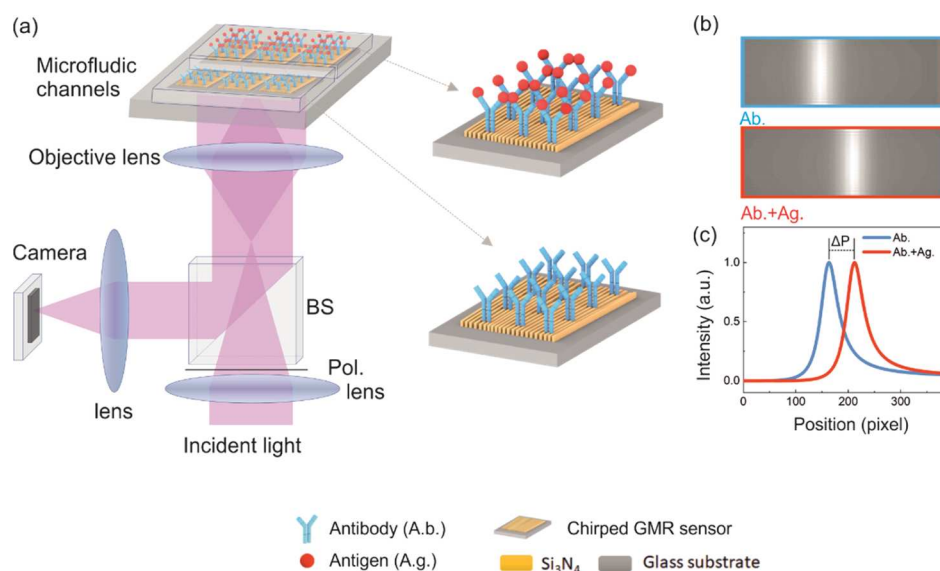
In order to provide a fair comparison of these methods, we applied them to the same datasets obtained with two different

**Figure 1.** Illustration of the chirped GMR biosensing method. (a) GMR sensors surface functionalized with antibodies, integrated into a microfluidic system with signal and reference channel to enable drift subtraction. The chip is illuminated with a polarized collimated beam. The middle figures show the scenario before and after the antigen binds to the antibody. (b) Camera image of the GMR sensor before and after binding takes place. (c) Corresponding resonance curves before and after binding. The curves are fitted and the change in peak position is recorded in terms of camera pixel shift ΔP. The value of ΔP is translated into a refractive index change and an antigen concentration using appropriate calibration measurements.
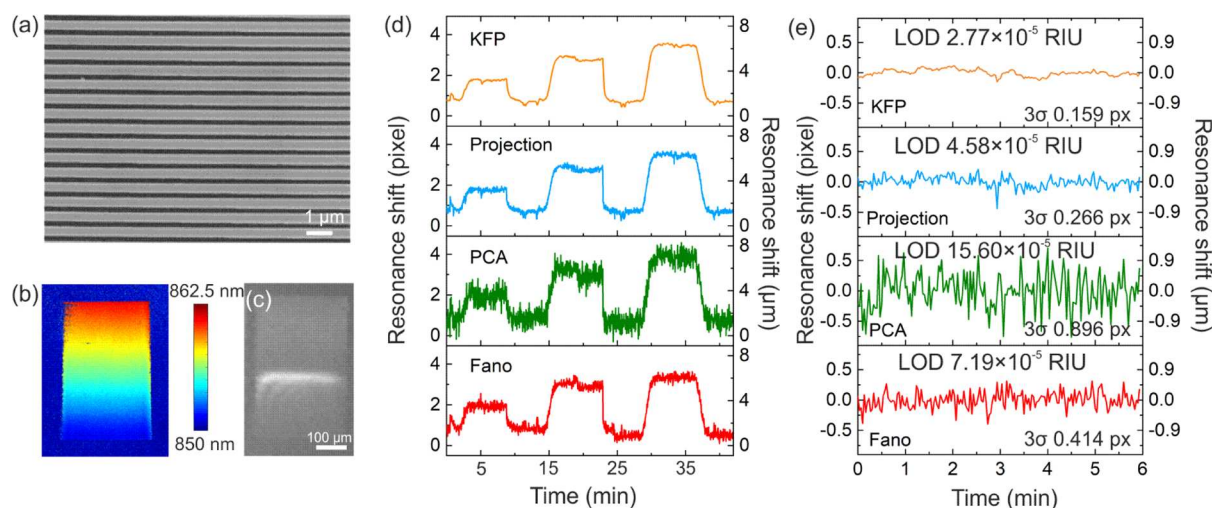

Figure 2. Bulk refractive index measurements of the chirped GMR. (a) Scanning electron microscopic image and (b) hyperspectral image of a chirped GMR sensor. (c) Charge-coupled device image of the chirped GMR when exposed to deionized (DI) water. (d) Refractive index over time for NaCl solutions of different concentrations. The corresponding RIs of the NaCl solutions measured using a commercial refractive index meter are 1.3334, 1.3338, and 1.3340. DI water was used as the reference and its RI is 1.3330. (e) 3σ value extracted from different fitting methods.

sensing modalities, that is, both high- and low-quality factor systems, represented by microrings ($Q \approx 4800$ and $13{,}000$) and a GMR ($Q \approx 150$), respectively. The silicon microring is read out via a standard spectrometer, while the GMR is made up of gratings with a gradually changing period, which we refer to as "chirped" GMR.[15] Chirping the period encodes spectral information into spatial information, which removes the need for a spectrometer and replaces it with a simple camera; the resulting readout is a bright bar that moves laterally as a function of the refractive index change, so the position of the bar provides the readout of the sensor (Figure 1). In the case of the microring, the spectrum is fitted with a Lorentzian curve in order to determine the refractive index change, while in case of the GMR, we fit a Fano function. The Fano function arises

as a result of interference between the Fabry−Perot resonance of the thin film waveguide and the resonant Bragg scattering process of the periodic structure. Both the Lorentzian and Fano functions are then tracked as the measurement progresses.

In addition to comparing the published methods, we explored further improvements, also taking computational overhead into account in view of the drive towards low-cost point-of-care sensors. To this end, we investigated the Kalman filter (KF) paradigm, which was first developed in the context of the Apollo lunar missions.[18,19] The KF is an efficient algorithm to minimize estimation errors and to reduce the impact of noise. The algorithm is a predictor-corrector type estimator, that is, it takes both the system and measurement
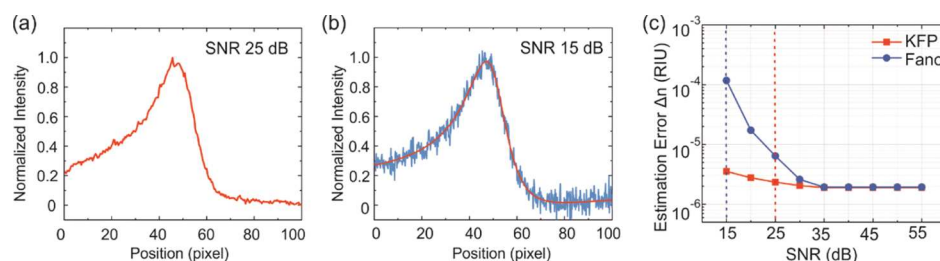
Figure 3. Impact of SNR on the LOD. (a) Typical measurement taken from the GMR dataset with an SNR of 25 dB. (b) Ideal data (red curve) with additional white Gaussian noise superimposed (blue curve), reducing the SNR to 15 dB. (c) Comparison of the LOD as a function of SNR for the Fano fit and KFP. The red dashed curve corresponds to the 25 dB curve of (a) and the blue dashed line corresponds to the 15 dB in (b).

noise into consideration when extracting information from noisy or uncertain data.[20] Its major advantage is the ability to infer the full probability distribution of the states and the parameters instead of making a simple point estimate. To date, much effort has been made to apply the KF to track moving objects[21] and to estimate parameters in biological systems interactions,[22−25] but has not yet been used to track real-time label-free biosensing data. In order to use the KF in the biosensing domain, we require prior knowledge of binding and unbinding events, such as association/dissociation constants (k_a/k_d), the concentration of unknown samples and the maximum response of the sensor. These parameters often vary considerably because of environmental conditions, for example, k_a and k_d may vary by more than an order of magnitude for the same protein affinity binding event,[26−29] so they cannot be assumed to be fixed values. Instead, they can be determined from the binding data using dynamic tracking (DT).[30,31] In fact, we realized that all of the unknown parameters, which also include solution concentration and maximum response of the sensor, can be determined iteratively. Therefore, here we present an extended KF (EKF) strategy based on an adaptive optimization procedure to determine all of these parameters directly from the data.

Using this EKF projection method (EKFP), we demonstrate an 80-fold reduction in the 3σ noise value of a low concentration (1 pg/mL) protein−protein binding assay.

■ RESULTS AND DISCUSSION

Comparison of Fitting Methods for Bulk RI Sensing on Chirped GMR. In this section, we present the comparison of described methods for the application to GMR data. A SEM micrograph of the GMR sensor is depicted in Figure 2a. As explained before, the resonance wavelength shifts with a continuous change in period. This effect is demonstrated in Figure 2b, where the resonance wavelength is depicted as a function of position in false colour. The wavelength range is displayed from 850 to 862.5 nm over a length of 500 μm. As represented in Figure 2d, in order to calibrate the sensitivity S of the sensor chip, we exposed it to NaCl solutions of different concentrations. As can be observed from Figure 2c, the resonance appeared as a bright bar in the captured image. Together with the standard deviation σ of the noise taken for a constant refractive index (Figure 2e), we determined the LOD as $3\sigma/S$ and compared the values for four methods, that is, Fano, PCA, projection, and KF projection (KFP). All measurements were repeated three times. KFP shows the lowest LOD (2.77×10^{-5} RIU) with a standard deviation of 6.75×10^{-6} RIU, which represents an almost threefold improvement over the conventionally used Fano method

(LOD 7.19×10^{-5} RIU) with a standard deviation of 1.09×10^{-5} RIU.

Initially, we had expected the PCA method to be superior because it collects more information, yet it showed a very similar, in fact, a higher, noise level than that of the original Fano method. We believe that this higher noise level originates from the imperfection of the Fano shape profile in successive measurements, which is not sufficiently constant. By using the lithographically tuned chirped GMR, it is expected that the different Fano curves would be nominally identical and simply shifted, but this is clearly not the case. The distortion of the respective curves due to noise is sufficient to violate the assumption of a constant shift and the PCA-based approach via lithographic tuning is therefore not viable, as shown in Supporting Information Section 6 and Figure S1.

Impact of the Signal-to-Noise Ratio on Fitting Accuracy. The generally accepted figure of merit for a resonant refractive index biosensor includes both the sensitivity S and the Q-factor, but not the signal-to-noise ratio (SNR) of the resonance curve, even though it appears obvious that a larger SNR should produce a better measurement. Here, we investigate the impact of the SNR on the LOD as a function of the fitting method.

We simulated the spectral responses using rigorous coupled-wave analysis (RCWA) for 10 different RIs at intervals of 10^{-5} RIU to verify the estimation error of the different algorithms in determining the RI as a function of added noise. Figure 3a,b represents the resonance profile for 15 and 25 dB at a defined RI. The average value of the absolute differences to the known RI was plotted against the level of noises in terms of SNR (Figure 3c).

We note that for all SNR values below 35 dB, the Kalman-based projection method outperforms the Fano-fit method. Considering real experimental conditions, the SNR is typically between 15 and 25 dB, which suggests that KFP outperforms Fano in all practical cases. We believe that the reason for this better performance is that KFP is a convolution operation combined with a parabolic fit. In contrast, the Fano fit relies on linear regression, which requires five parameters to be optimized for convergence; it is also recognized that a parabolic operation typically has a smaller estimation error than a linear operation.[32] Moreover, we have investigated the impact of various sources of noise on the performance of resonant refractive index sensors, for example, camera noise and light source noise, with the result that the noise induced by the camera is the major limitation, while intensity noise of the light source is mitigated by the fitting of a resonance curve.[33]

Comparison of Fitting Methods for Bulk RI Sensing on the Microring Resonator. The results for the chirped GMR demonstrate that the KF-based projection method
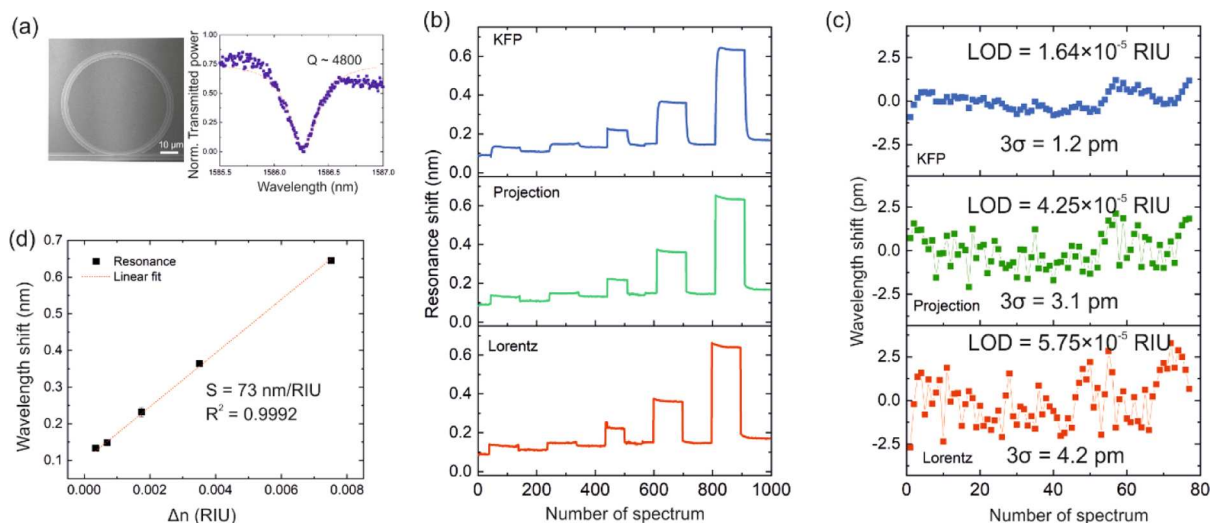
Figure 4. Bulk sensitivity measurement for the microring resonator with a Q of 4800. (a) SEM and normalized transmitted spectrum of the microring. (b) Resonance shift with respect to DI water which was estimated by Lorentz fit, projection, and KFP method. (c) 3σ value extracted from different fitting methods. The corresponding RIs of the NaCl solutions measured using a commercial refractive index meter are 1.3334, 1.3337, 1.3348, 1.3365, and 1.3405. DI water was used as the reference and its RI is 1.3330. (d) Sensitivity curve obtained from the measurement.
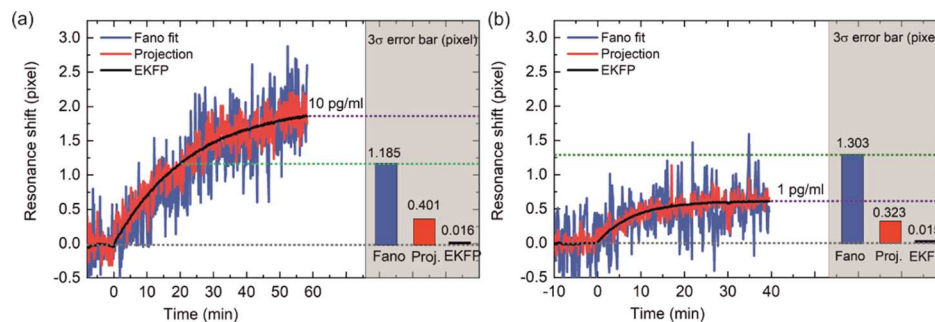
Figure 5. CRP antibody−antigen binding in a urine matrix. The blue, red, and black curves represent the response of chirped GMR processed by the Fano fit and the projection and EKFP method, respectively. The corresponding error bars are in the same colour. The concentrations of CRP antigen are (a) 10 and (b) 1 pg/mL in urine. The 3σ value for the Fano fit, projection, and EKFP is 1.185, 0.401, and 0.016 pixels for 10 pg/mL CRP and 1.303, 0.323, and 0.015 pixels for 1 pg/mL CRP. Note that 1 pixel corresponds to 1.82 μm in this case.

improves the data analysis for sensors with low Q resonances. To explore the possibilities for a sensor with high Q values, we analyzed the data accumulated with two silicon microring resonators with a Q-factor of 4800 (Figure 4) and 13,000 (Figure S4). As before, we exposed the sensor to NaCl solutions of different concentrations and analyzed the noise. Because of the much lower free spectral range of the microring compared to the GMR, multiple resonances are clearly apparent in the measurement window (Figure S4a), which we used for PCA and compared with other algorithms (Section 9, Supporting Information).

As demonstrated in Figure 4c, the KFP method reduces the 3σ from 4.2 to 1.2 pm and enhances the LOD from 5.75 × 10^{-5} to 1.64 × 10^{-5} RIU, compared to the Lorentz fit. Similar bulk sensitivity measurements were carried out on another microring with a Q factor of 13,000. Similar results (Figure S4) were obtained as before. KFP method consistently reduces the 3σ for both low- and high-Q devices (Figure S6).

Measurement of CRP Antibody and Antigen Binding Event. Finally, we applied the EKFP method to analyze the data accumulated from protein affinity binding measurements, in particular the detection of human C-reactive protein (CRP) in urine. Recall that the "E" in the acronym refers to "extended", which refers to the fact that the binding constants

and analyte concentration are determined iteratively. CRP antibodies were immobilized on the sensor surface and the sensor exposed to CRP, as described in previous work.[34] The binding curves for 10 and 1 pg/mL CRP are shown in Figure 5a,b. The data were analyzed using the Fano fit and the projection and EKFP methods.

As shown in Figure 5a, for 10 pg/mL CRP, the 3σ using the Fano fit method is 1.185 pixels, while the resonance shift is estimated to be 1.853 pixels. This is just above the noise level and the measurement is close to the LOD.[34] In fact, for the first 20 min, the signal is buried in the noise. In comparison, the projection method outputs a much smaller 3σ (0.401 pixels) that is well below the final resonance shift (1.853 pixels) and consequently produces an improved detection limit. The further advantage of the EKFP over Fano fit is evident, where the calculated 3σ is 0.016 and 1.185 pixels, respectively. The low noise of the EKFP method enables the direct and accurate readout of resonance shift for a real-time measurement. More importantly, it enables us to fully capture the time dependence of the binding curve, which provides additional information in the context of DT.[30,31]

An interesting aspect to consider is if the EKFP method would allow us to resolve an even lower concentration of CRP which was previously undetectable. Therefore, we prepared 1

pg/mL CRP antigen solution and tested it in the same setup. From Figure 5b, it is very clear that the 3σ value of the Fano fit is much higher than the resonance shift of 1 pg/mL, so the resonance shift obtained by the Fano fit is buried in the noise and hence not resolvable; in contrast, the EKFP method reduces the 3σ value to 0.015 pixels, which is about 86 times lower than that of the Fano fit ($3\sigma = 1.303$ pixels). To be noted, the reduction of 3σ for the EKFP method is different to that of the KFP method because different state space functions are used. For the CRP binding measurement, the EKFP method used a Langmuir isotherm, while for the bulk RI measurement, the KFP method employed the constant state space function.

It is also important to consider the computational cost for the algorithms. As is well known, KFs are extremely efficient because of their recursive nature. The computational complexity is dominated by $O(CN)$, where N is the number of examples and C is the number of parametric variables. The only computation part of the EKFP method is the projection part. As has already been pointed out,[17] the computational complexity of the projection method is $O(pN)$, where p is the number of reference spectra and N is the number of wavelength samples. In this case, where $p = 40$, the computational complexity is $O(40N)$, while for the Fano fit, the algorithm is based on the least squares regression with N examples and C parametric variables, the total computational complexity is $O(C^2N)$.[19] In this case, the computational complexity is $O(25N)$. For PCA, the computational complexity is $O(N^3)$ which is one order of magnitude higher than for the other algorithms. In conclusion, EKFP and the projection method share a similar computational complexity, they can run in real time, and could also run real-time on a much less powerful microprocessor.

Overall, the superiority of the EKFP method over the simple Fano fit and projection methods is demonstrated, especially for the case of low-Q resonant biosensors. The remaining limitations are the restriction of the camera resolution (the number of pixels), temperature fluctuations, and mechanical noise during the experiment; for example, a thermal noise of 0.1 °C can easily occur, which may result in a $\Delta n = 1.0 \times 10^{-5}$ RIU variation.[35−37] Although the system has a reference channel to minimize the impact of such variations, differences between the signal and reference channel cannot be totally avoided.

■ CONCLUSIONS

In conclusion, we have introduced a KF method to the interpretation of biosensor data and have compared it to other curve-fitting methods. This method combines the error variance from the measured data with the predicted value through a kinetic model, and updates the error variance recursively. We have demonstrated that both in a low-Q system (a GMR with $Q \approx 150$) and in a high-Q system (microring with $Q \approx 4800$ and $13{,}000$), the Kalman projection method can reduce the 3σ by a factor 2 to 3 compared to the Fano fit or Lorentz fit. In comparison, the PCA-based method did not exhibit a good performance either for lithographically tuned GMR or for microring resonator data, indicating that the stringent requirements of PCA limit its application in the context of the sensor modalities examined here. We also applied an extended KF method termed EKFP, which allows determining the affinity kinetics iteratively to a urinary CRP antibody−antigen binding experiment. The EKFP method

significantly improves the SNR and lowers the LOD of the CRP affinity binding interaction from 10 down to 1 pg/mL, which highlights the potential of this method for real protein−protein binding measurements. In addition, it is worth mentioning that for a nonlinear process, a non-Gaussian error distribution, or a quickly varying process, the EKF with linearization via first order Taylor expansion may only provide a poor estimation. In that case, a Monte Carlo KF or a particle filter[38] method may provide a better estimation. Overall, we have shown that applying the KF algorithm improves the fitting of biosensor data both for raw image data and for spectral data, and the algorithm can easily be adapted to other sensing modalities, such as angle scanned SPR.

■ METHODS

Kalman Filtering Technique. The KF algorithm is practiced as a two-step algorithm; as the first step, it generates a time domain update for the prediction and for the final step, it produces a measurement update for the correction. We also developed an EKF to account for the antibody−antigen binding interaction. The EKF we introduce adds an iterative determination of the association/dissociation constants (k_a/k_d) and the concentration of the unknown sample as an additional step in order to make the method more suitable for biosensing.

KF for Bulk RI Measurement. The resonance response of the chirped GMR to a fixed concentration of NaCl solution can be considered as static because the RI of NaCl solution is constant for a given concentration and the only variation is provided by factors such as temperature and mechanical noises. The expected refractive index of the current state $\hat{x}_k^-$ should therefore be the same as that of the previously estimated state $\hat{x}_{k-1}^-$, so the state function at time $k - 1$ and k is identical

$$\hat{x}_k^- = \hat{x}_{k-1}^- \tag{1}$$

The prior predicted error covariance P_k^- at time k is defined as the summation of the error covariance P_{k-1} at time $k - 1$ and the process error covariance Q which reflects the noises on the measurement system, for example, temperature and mechanical vibration. Here, we assume Q to be Gaussian distributed white noise.

$$P_k^- = P_{k-1} + Q \tag{2}$$

The Kalman gain G_k is then calculated as

$$G_k = \frac{P_k^-}{P_k^- + R} \tag{3}$$

where R is the estimated measurement error covariance. The state eq 1 is then updated accordingly

$$\hat{x}_k = \hat{x}_k^- + G_k(z_k - \hat{x}_{k+1}^-) \tag{4}$$

where $\hat{x}_k$ is the estimated state at time k and z_k is the measurement value at time k. The error covariance P_k is updated as

$$P_k = (1 - G_k)P_k^- \tag{5}$$

EKF with a Langmuir Isotherm Model for Antigen−Antibody Binding Interaction. Antigen−antibody binding interaction is a complex dynamic process. When the antigen binds to the antibody, it forms a binding complex and the rate of binding is described by the association constant k_a. Once bound, the disassociation process, described by k_d, starts to happen, releasing the antigen again. This dynamic interaction can be simplified by the Langmuir isotherm model,[39,40] which describes how a ligand molecule interacts with an analyte molecule. The complex formed by the ligand and the antigen follows pseudo-first-order kinetics and it is assumed that the binding is equivalent and independent for all binding sites. The response Y_t from the sensor is proportional to the mass of the bound complex and can be expressed as[41]

$$\frac{dY_t}{dt} = k_a[Ag](Y_{max} - Y_t) - k_d Y_t \tag{6}$$

where k_a is the association constant, k_d is the dissociation constant, [Ag] is the antigen concentration, and Y_{max} is the maximum value of the sensor readout which happens at the equilibrium state. Integrating eq 6, we obtain the response of the sensor as a function of time t

$$Y(t) = \frac{Y_{max}[Ag]}{K_D + [Ag]}(1 - e^{-(k_a[Ag]+k_d)t}) \tag{7}$$

where K_D is the ratio of dissociation constant k_d over the association constant k_a. From eq 7, the response of sensor Y is continuous and is differentiable at time t, so it can be expressed by a first-order Taylor expansion as

$$Y(t + \Delta T) = Y(t) + s(t)\Delta T \tag{8}$$

where ΔT is the time interval and $s(t)$ is the derivative of Y

$$s(t) = \frac{\partial Y_t}{\partial x_t} \tag{9}$$

$s(t)$ is also called the Jacobian matrix and usually noted as matrix F at discrete time step k

$$F_k = \frac{\partial Y_k}{\partial x_k} = \frac{\partial}{\partial x_k}\left(\frac{Y_{max}[Ag]}{K_D + [Ag]}(1 - e^{-(k_a[Ag]+k_d)x_k})\right)$$

$$= \frac{Y_{max}[Ag](k_a[Ag] + k_d)}{K_D + [Ag]}e^{-(k_a[Ag]+k_d)x_k} \tag{10}$$

The state vector of the state-space dynamic model is $x = [Y, s]^T$. If the response is measured at every ΔT, then according to eq 8, the true state vector x_{k+1} at time step $k + 1$ can be determined from the value x_k given at step k using a linear stochastic difference model

$$x_{k+1} = Ax_k + w_k \tag{11}$$

where

$$A = \begin{bmatrix} 1 & \Delta T \\ 0 & 1 \end{bmatrix} \tag{12}$$

and w_k represents the process noise. From eq 6, the state function estimation relies on parameters k_a and k_d, concentration of the antigen [Ag], and the sensor maximum response Y_{max}. There are many methods[42−45] to determine k_a and k_d beforehand, but the lack of information about the unknown concentration of antigen [Ag] and the value of Y_{max} is the main obstacle for the EKF method to make precise prediction based on the state-space equation alone. Therefore, we employ an optimization function O (eq 13) by minimizing the difference of measured data and the Langmuir model through nonlinear least square solver.[19] The abovementioned parameters could be extracted from the kinetic model with the highest confidence.

$$O = \min \sum \|f(i) - y(i)\| \tag{13}$$

where $f(i)$ is the nonlinear function and $y(i)$ is the measured data Y_k.

$$f(k_a, k_d, y_{max}) = \frac{y_{max}[Ag]}{k_d/k_a + [Ag]}(1 - e^{-(k_a[Ag]+k_d)k}) \tag{14}$$

Because Y is the output (resonance position) of the sensor at time step k, the observation vector z_k of the state-space dynamic model can be expressed as

$$z_k = h(x_k) + v_k = x_k + v_k \tag{15}$$

where v_k represents the measurement noise determined as the standard deviation of the resonance position. In this case, there is no unit transformation, so $h = 1$. Equations 9 and 15 constitute the state and observation equations, respectively. Note that the variables w_k and v_k correspond to the covariance of σ_w^2 and σ_v^2, respectively. The covariance matrices of w_k and v_k are

$$Q_k = \begin{bmatrix} 0 & 0 \\ 0 & \sigma_w^2 \end{bmatrix} \text{ and } R_k = [\sigma_v^2] \tag{16}$$

where σ_w^2 is the process noise, which is hidden in the process. It can be treated as a tuning parameter to adjust the gain of the KF to smooth the data. The determination of σ_w^2 is quite subjective, but it can be estimated via numerical simulations in different test environments[21] or through adaptive adjustment.[46] With the above-mentioned state-space dynamic model, the EKF time update equations and measurement update equations are presented in three group of functions: the state space eqs 17 and 18, the predict eqs 19−21, and the update eqs 22 and 23

$$\hat{x}_{k+1}^- = A\hat{x}_k + w_k \tag{17}$$

$$z_k = x_k + v_k \tag{18}$$

$$P_{k+1}^- = F_k P_k F_k^T + Q_k \tag{19}$$

$$G_{k+1} = P_{k+1}^- H^T (H P_{k+1}^- H^T + R)^{-1} \tag{20}$$

$$F_k = \frac{\partial f}{\partial x} \quad H_k = \frac{\partial h}{\partial x} \tag{21}$$

$$\hat{x}_{k+1} = \hat{x}_{k+1}^- + G_{k+1}(z_{k+1} - h(\hat{x}_{k+1})) \tag{22}$$

$$P_{k+1} = (1 - G_{k+1}H)P_{k+1}^- \tag{23}$$

where $\hat{x}_{k+1}$ is the a posteriori state estimate, $\hat{x}_{k+1}^-$ is the a priori state estimate, P_{k+1}^- and P_{k+1} denote the a priori estimate error covariance and the a posteriori estimate error covariance, respectively, and G_{k+1} is the Kalman gain matrix.

In summary, the EKF process can be described as follows: first, the parameters are initialized in eq 14 and then the parameters k_a, k_d, [Ag], and Y_{max} are extracted using the data for time steps between 0 and $t - 1$. Typically 25 iterations are sufficient to reach 95% confidence intervals. Then the optimized parameters are passed to eq 7 to predict the sensor response at time t. Then, eqs 17 and 19 project the current state and covariance estimates, respectively. Subsequently, the output of eq 18 is considered to update eqs 19−23. The algorithm operates recursively by continuously updating eqs 13 and 14.

Projection Method. The single and double projection methods were initially described in refs.[16,17] In brief, the double projection method is an eigenvector analysis, which uses singular value decomposition to create a basis for each simulated spectrum at different RIs. Then each simulation is projected against the basis to form a weight matrix. The inverse problem of calculating the refractive index from the spectrum can be solved as follows: first, convert the spectrum into a vector and then project the vector to the basis to form a weight vector. Finally, project the weight vector to each row of the weight matrix to obtain the solution vector. The abscissa of the interpolated maxima will correspond to the desired unknown index of refraction.

The single projection method eliminates the content of the eigenvector analysis and directly projects the normalized reflectance spectrum T to the simulated reflectance spectrum at different RIs. Then the abscissa of the interpolated maxima represents the unknown index of refraction.

The single projection method can be seen as a convolution operation; therefore, its computational complexity scales as $\sim O(pN)$ where p is the number of reflectance images and N is the number of wavelength samples. In contrast, the computational complexity of the double projection method scales as $\sim O(N^3)$. For a large number of samples, the value of $O(N^3)$ becomes much larger than $O(pN)$, which is undesirable. Therefore, we compared the two methods on the same dataset of bulk RI measurements of NaCl solutions to find out whether the computational overhead of the double projection method was worth the effort. Surprisingly, we found that the average 3σ for the double projection and single projection methods for this dataset was 0.2823 and 0.2919 pixel, respectively, as shown in Figure S3, so the two methods exhibit a similar estimation error. Because the

double projection method exhibits slightly lower noise, we use it in the remainder of the paper and simply refer to it as the "projection method".

Principal Component Analysis. Owing to the property of rejecting noise and improving SNR, for example, Raman spectroscopy,[13] we also include PCA in our comparison. Similar to the projection method, PCA is also based on singular value decomposition whereby a covariance matrix is calculated, which is followed by the calculation of eigenvectors of the same matrix. These eigenvectors are known as principal components which represent the presence of maximal variance in the dataset. In order to apply PCA to the chirped-GMR dataset, one would require a high-precision tunable light source for sweeping the wavelength[13,14] The change in the spectrum with respect to wavelength would then be represented by the first principal component with the largest eigenvalue, which could be discriminated against the noise (Supporting Information Section 1). For our target application of a low-cost point-of-care sensor, however, it would be impractical to include a high precision tunable light source. Hence, we generate the wavelength-swept data by lithographic tuning, which allows us to capture it in a single measurement. The PCA algorithm is then applied to the lithographically tuned GMRs (several GMRs with a small resonance difference of $\Delta\lambda = 0.1$ nm) and the resonance matrix is built from this data. The procedure is described in the Supporting Information Section 6 and Figure S1.

For the microring resonator, PCA is applied as follows; first, the transmission spectrum is cropped into identical width, by keeping the resonance dip at the center. Each dip profile is then shifted by equal space with an optimized step size (2 data points) after centralization. Then high-frequency variations (which are not characteristic of resonance) in the spectra are removed using a lowpass filter with an optimized sampling frequency of 4 Hz. The resulting smooth spectra are then normalized to remove any intensity fluctuations. A covariance matrix is calculated from these normalized spectra, followed by the calculation of the corresponding eigenvectors. Finally, a derivative Lorentz function is applied to fit the first principal component (PC1). The resonance position is extracted as the zero crossing point of the derivative function. More details are shown in the Supporting Information Section 8 and Figure S2.

Simulation of Chirped GMR. The response of the chirped GMR is simulated in a staircase approximation with a 0.5 nm change in period. The RCWA[47,48] method is used to calculate the spectrum and the phase profile, and a set of resonant images are created.

Fabrication. The fabrication of GMR and microring structures, as well as the microfluidic channels, is already described in our previous work.[15,34,49] Briefly, the chirped GMR is created by tuning the GMR period in 1 nm steps, which is limited by the smallest step size of our Raith VOYAGER electron-beam lithography tool. We increase the period from 575 to 585 nm over a 500 μm length with a fill factor of 0.7 to achieve a resonance around 855 nm in the center of the chirped GMR. The gratings are fabricated on a Si_3N_4-on-glass wafer (Silson Ltd), with a Si_3N_4 layer of 150 nm thickness. The microring structure consists of a 500 nm-wide and 220 nm-thick waveguide with a ring diameter of 60 μm and is designed to work around 1570 nm. The microfluidic channel is fabricated using the polydimethylsiloxane replica mold method.

Sensor Functionalization. The GMR sensor surface functionalization was described in detail in our previous work.[34] Briefly, the sensor surface was first treated with piranha solution and then salinized with (3-mercaptopropyl)trimethoxysilane (MPTS). After drying the surface, the sensor is immersed in $SM(PEG)_6$ in DMSO before the CRP antibody binding.

Bulk RI Measurements by Sensors. The bulk RI measurements for the chirped GMR and the microring are described in detail in the Supporting Information. In brief, the bulk RI and protein binding experiments for the GMR were both carried out on a bespoke microscope setup with the microfluidic channels bonded to the sensor surface. The bulk RI measurement for the microring was carried out on a fire-end system to collect the transmission spectrum.

ASSOCIATED CONTENT

Ⓢ Supporting Information

The Supporting Information is available free of charge at https://pubs.acs.org/doi/10.1021/acssensors.0c01484.

> PCA, Fano function, Lorentz function, derivative Lorentz function; bulk RI measurement by sensors; illustration of the PCA approach for lithographically tuned chirped GMR; illustration of the PCA-based approach for the microring resonator; comparison of the double projection and single projection method; bulk sensitivity measurement for the microring resonator with a Q of 13,000; illustration of subpixel resolution; and comparison of 3σ for GMR and the microring resonator (PDF)

AUTHOR INFORMATION

Corresponding Author

Kezheng Li − *Department of Physics, University of York, York YO10 5DD, U.K.;* ⓞ orcid.org/0000-0002-9234-3312; Email: kezheng.li@york.ac.uk

Authors

Roopam Gupta − *SUPA, School of Physics and Astronomy and School of Medicine, University of St Andrews, Andrews KY16 9SS, U.K.*

Alexander Drayton − *Department of Physics, University of York, York YO10 5DD, U.K.*

Isabel Barth − *Department of Physics, University of York, York YO10 5DD, U.K.*

Donato Conteduca − *Department of Physics, University of York, York YO10 5DD, U.K.*

Christopher Reardon − *Department of Physics, University of York, York YO10 5DD, U.K.*

Kishan Dholakia − *SUPA, School of Physics and Astronomy, University of St Andrews, Andrews KY16 9SS, U.K.; Department of Physics, College of Science, Yonsei University, Seoul 03722, South Korea*

Thomas F. Krauss − *Department of Physics, University of York, York YO10 5DD, U.K.;* ⓞ orcid.org/0000-0003-4367-6601

Complete contact information is available at:
https://pubs.acs.org/10.1021/acssensors.0c01484

Author Contributions

This manuscript was written through contributions of all authors. All authors have given approval to the final version of the manuscript.

Notes

The authors declare no competing financial interest.

REFERENCES

(1) Liedberg, B.; Nylander, C.; Lundström, I. Biosensing with surface plasmon resonance - how it all started. *Biosens. Bioelectron.* **1995**, *10*, i−ix.

(2) De Vos, K.; Bartolozzi, I.; Schacht, E.; Bienstman, P.; Baets, R. Silicon-on-Insulator microring resonator for sensitive and label-free biosensing. *Opt. Express* **2007**, *15*, 7610.

(3) Herranz, S.; Gavela, A. F.; Lechuga, L. M. Label-Free Biosensors Based on Bimodal Waveguide (BiMW) Interferometers. In *Biosensors and Biodetection. Methods in Molecular Biology*; Rasooly, A., Prickril, B., Eds.; Humana Press: New York, 2017; Vol. *1571*; p 161.

(4) Estevez, M. C.; Alvarez, M.; Lechuga, L. M. Integrated optical devices for lab-on-a-chip biosensing applications. *Laser Photonics Rev.* **2012**, *6*, 463−487.

(5) Mariani, S.; Robbiano, V.; Strambini, L. M.; Debrassi, A.; Egri, G.; Dähne, L.; Barillaro, G. Layer-by-layer biofunctionalization of nanostructured porous silicon for high-sensitivity and high-selectivity label-free affinity biosensing. *Nat. Commun.* **2018**, *9*, 5256.

(6) Shamah, S. M.; Cunningham, B. T. Label-free cell-based assays using photonic crystal optical biosensors. *Analyst* **2011**, *136*, 1090−1102.

(7) Wang, S. S.; Magnusson, R. Theory and applications of guided-mode resonance filters. *Appl. Opt.* **1993**, *32*, 2606−2613.

(8) Tsai, M.-Z.; Hsiung, C.-T.; Chen, Y.; Huang, C.-S.; Hsu, H.-Y.; Hsieh, P.-Y. Real-time CRP detection from whole blood using micropost-embedded microfluidic chip incorporated with label-free biosensor. *Analyst* **2018**, *143*, 503−510.

(9) Barth, I.; Conteduca, D.; Reardon, C.; Johnson, S.; Krauss, T. F. Common-path interferometric label-free protein sensing with resonant dielectric nanostructures. *Light: Sci. Appl.* **2020**, *9*, 96.

(10) Nenninger, G. G.; Piliarik, M.; Homola, J. Data analysis for optical sensors based on spectroscopy of surface plasmons. *Meas. Sci. Technol.* **2002**, *13*, 2038−2046.

(11) Johnston, K. S.; Booksh, K. S.; Chinowsky, T. M.; Yee, S. S. Performance comparison between high and low resolution spectrophotometers used in a white light surface plasmon resonance sensor. *Sens. Actuators, B* **1999**, *54*, 80−88.

(12) Stenberg, E.; Persson, B.; Roos, H.; Urbaniczky, C. Quantitative determination of surface concentration of protein with surface plasmon resonance using radiolabeled proteins. *J. Colloid Interface Sci.* **1991**, *143*, 513−526.

(13) Mazilu, M.; De Luca, A. C.; Riches, A.; Herrington, C. S.; Dholakia, K. Optimal algorithm for fluorescence suppression of modulated Raman spectroscopy. *Opt. Express* **2010**, *18*, 11382−11395.

(14) De Luca, A. C.; Mazilu, M.; Riches, A.; Herrington, C. S.; Dholakia, K. Online Fluorescence Suppression in Modulated Raman Spectroscopy. *Anal. Chem.* **2010**, *82*, 738−745.

(15) Triggs, G. J.; Wang, Y.; Reardon, C. P.; Fischer, M.; Evans, G. J. O.; Krauss, T. F. Chirped guided-mode resonance biosensor. *Optica* **2017**, *4*, 229−234.

(16) Alleyne, C. J.; Kirk, A. G.; Chien, W.-Y.; Charette, P. G. Numerical method for high accuracy index of refraction estimation for spectro-angular surface plasmon resonance systems. *Opt. Express* **2008**, *16*, 19493−19503.

(17) Abumazwed, A.; Kubo, W.; Shen, C.; Tanaka, T.; Kirk, A. G. Projection method for improving signal to noise ratio of localized surface plasmon resonance biosensors. *Biomed. Opt. Express* **2017**, *8*, 446−459.

(18) Kalman, R. E. A New Approach to Linear Filtering and Prediction Problems. *J. Basic Eng.* **1960**, *82*, 35−45.

(19) https://uk.mathworks.com/help/optim/nonlinear-least-squares-curve-fitting.html (accessed Apr 19, 2020).

(20) Wilkinson, D. J. Bayesian methods in bioinformatics and computational systems biology. *Briefings Bioinf.* **2007**, *8*, 109−116.

(21) Tao, L.; Liu, Z.; Zhang, W.; Zhou, Y. Frequency-scanning interferometry for dynamic absolute distance measurement using Kalman filter. *Opt. Lett.* **2014**, *39*, 6997−7000.

(22) Murtuza Baker, S.; Poskar, C. H.; Schreiber, F.; Junker, B. H. An improved constraint filtering technique for inferring hidden states and parameters of a biological model. *Bioinformatics* **2013**, *29*, 1052−1059.

(23) Lillacci, G.; Khammash, M. Parameter Estimation and Model Selection in Computational Biology. *PLoS Comput. Biol.* **2010**, *6*, No. e1000696.

(24) Sun, X.; Jin, L.; Xiong, M. Extended Kalman Filter for Estimation of Parameters in Nonlinear State-Space Models of Biochemical Networks. *PLoS One* **2008**, *3*, No. e3758.

(25) Facchinetti, A.; Sparacino, G.; Cobelli, C. Enhanced accuracy of continuous glucose monitoring by online extended kalman filtering. *Diabetes Technol. Ther.* **2010**, *12*, 353−363.

(26) Yen, Y.-K.; Lai, Y.-C.; Hong, W.-T.; Pheanpanitporn, Y.; Chen, C.-S.; Huang, L.-S. Electrical Detection of C-Reactive Protein Using a Single Free-Standing, Thermally Controlled Piezoresistive Micro-cantilever for Highly Reproducible and Accurate Measurements. *Sensors* **2013**, *13*, 9653−9668.

(27) Fan, Y.-J.; Sheen, H.-J.; Liu, Y.-H.; Tsai, J.-F.; Wu, T.-H.; Wu, K.-C.; Lin, S. Detection of C-Reactive Protein in Evanescent Wave Field Using Microparticle-Tracking Velocimetry. *Langmuir* **2010**, *26*, 13751−13754.

(28) Bíró, A.; Rovó, Z.; Papp, D.; Cervenak, L.; Varga, L.; Füst, G.; Thielens, N. M.; Arlaud, G. J.; Prohászka, Z. Studies on the interactions between C-reactive protein and complement proteins. *Immunology* **2007**, *121*, 40−50.

(29) Olkhov, R. V.; Shaw, A. M. Quantitative label-free screening for antibodies using scattering biophotonic microarray imaging. *Anal. Biochem.* **2010**, *396*, 30−35.

(30) Sevenler, D.; Trueb, J.; Ünlü, M. S. Beating the reaction limits of biosensor sensitivity with dynamic tracking of single binding events. *Proc. Natl. Acad. Sci. U. S. A.* **2019**, *116*, 4129.

(31) Gopalan, D.; Nair, P. R. Dynamic Tracking Biosensors: Finding Needles in a Haystack. *ACS Sens.* **2020**, *5*, 1374−1380.

(32) Fisher, R. B.; Naidu, D. K. A Comparison of Algorithms for Subpixel Peak Detection. In *Image Technology*; Sanz, J. L. C., Ed.; Springer: Berlin, Heidelberg, 1996; pp 385−404.

(33) Drayton, A.; Li, K.; Simmons, M.; Reardon, C.; Krauss, T. F. Performance limitations of resonant refractive index sensors with low-cost components. *Opt. Express* **2020**, *28*, 32239.

(34) Kenaan, A.; Li, K.; Barth, I.; Johnson, S.; Song, J.; Krauss, T. F. Guided mode resonance sensor for the parallel detection of multiple protein biomarkers in human urine with high sensitivity. *Biosens. Bioelectron.* **2020**, *153*, 112047.

(35) Kurtz, S. S.; Amon, S.; Sankin, A. Effect of Temperature on Density and Refractive Index. *Ind. Eng. Chem.* **1950**, *42*, 174−176.

(36) Abbate, G.; Bernini, U.; Ragozzino, E.; Somma, F. The temperature dependence of the refractive index of water. *J. Phys. D: Appl. Phys.* **1978**, *11*, 1167−1172.

(37) Kim, Y. H.; Park, S. J.; Jeon, S.-W.; Ju, S.; Park, C.-S.; Han, W.-T.; Lee, B. H. Thermo-optic coefficient measurement of liquids based on simultaneous temperature and refractive index sensing capability of a two-mode fiber interferometric probe. *Opt. Express* **2012**, *20*, 23744−23754.

(38) Wang, X.; Li, T.; Sun, S.; Corchado, J. A Survey of Recent Advances in Particle Filters and Remaining Challenges for Multitarget Tracking. *Sensors* **2017**, *17*, 2707.

(39) Langmuir, I. THE CONSTITUTION AND FUNDAMENTAL PROPERTIES OF SOLIDS AND LIQUIDS. PART I. SOLIDS. *J. Am. Chem. Soc.* **1916**, *38*, 2221−2295.

(40) Latour, R. A. The langmuir isotherm: A commonly applied but misleading approach for the analysis of protein adsorption behavior. *J. Biomed. Mater. Res., Part A* **2015**, *103*, 949−958.

(41) Guo, H.; Zhou, X.; Zhang, Y.; Gu, C.; Song, B.; Shi, H. Kinetic analysis of a high-affinity antibody/antigen interaction performed by planar waveguide fluorescence immunosensor. *RSC Adv.* **2016**, *6*, 13837−13845.

(42) Frey, K. A.; Roger, L. A. Receptor binding techniques. *Curr. Protoc. Neurosci.* 2001, Chapter 1: Unit 1.4. DOI: 10.1002/0471142301.ns0104s00. PMID: 18428450.

(43) Capraro, B. R.; Shi, Z.; Wu, T.; Chen, Z.; Dunn, J. M.; Rhoades, E.; Baumgart, T. Kinetics of Endophilin N-BAR Domain Dimerization and Membrane Interactions. *J. Biol. Chem.* **2013**, *288*, 12533−12543.

(44) Kim, H. S.; Hage, D. S. Chromatographic analysis of carbamazepine binding to human serum albumin. *J. Chromatogr. B: Anal. Technol. Biomed. Life Sci.* **2005**, *816*, 57−66.

(45) Li, L.; Zhou, R.; Geng, H.; Yue, L.; Ye, F.; Xie, Y.; Liu, J.; Kong, X.; Jiang, H.; Huang, J.; Luo, C. Discovery of two aminoglycoside antibiotics as inhibitors targeting the menin-mixed lineage leukaemia interface. *Bioorg. Med. Chem. Lett.* **2014**, *24*, 2090−2093.

(46) Akhlaghi, S.; Zhou, N.; Huang, Z. Adaptive adjustment of noise covariance in Kalman filter for dynamic state estimation, *2017 IEEE Power & Energy Society General Meeting*, 16−20 July 2017, 2017; pp 1−5.

(47) Whittaker, D. M.; Culshaw, I. S. Scattering-matrix treatment of patterned multilayer photonic structures. *Phys. Rev. B: Condens. Matter Mater. Phys.* **1999**, *60*, 2610−2618.

(48) Popov, E.; Nevière, M. Maxwell equations in Fourier space: fast-converging formulation for diffraction by arbitrary shaped, periodic, anisotropic media. *J. Opt. Soc. Am. A* **2001**, *18*, 2886−2894.

(49) Juan-Colás, J.; Parkin, A.; Dunn, K. E.; Scullion, M. G.; Krauss, T. F.; Johnson, S. D. The electrophotonic silicon biosensor. *Nat. Commun.* **2016**, *7*, 12769.